Nanoscale

ROYAL SOCIETY OF CHEMISTRY

PAPER

View Article Online
View Journal | View Issue

Cite this: *Nanoscale*, 2025, **17**, 2871

Enhanced superhydrophobic robustness of black silicon employing nanojungle structures†

Lingju Meng, *[a,b,c] Mohammad Awashra, [b,c] Seyed Mehran Mirmohammadi, [b,c] Seyede Maryam Mousavi, [b] Jaana Vapaavuori, [b] Ville P. Jokinen [b,c] and Sami Franssila*[b,c]

Superhydrophobic surfaces are essential in various industries such as textiles, aviation, electronics and biomedical devices due to their exceptional water-repellent properties. Black silicon (b-Si) would be an ideal candidate for some applications due to its nanoscale topography made with a convenient lithography-free step and complementary metal–oxide-semiconductor (CMOS) compatible fabrication process. However, its use is hindered by serious issues with mechanical robustness. This study presents 'nanojungle b-Si', characterized by elongated and deep nanostructures and fabricated through photoresist micromasks associating with Bosch etching. These nanojungle structures exhibit enhanced robustness and sustain superhydrophobicity under abrasive conditions, outperforming traditional 'nanograss b-Si'. Optical analysis indicates that the nanojungle structures dissipate abrasive impact energy more effectively, preserving surface roughness and hydrophobicity. Notably, nanojungle b-Si maintains its superhydrophobicity even after impinging by 20 g of sand impacting from a height of 40 cm. This advancement in b-Si surfaces holds significant potential for enhancing future technological applications.

Received 12th October 2024,
Accepted 8th January 2025

DOI: 10.1039/d4nr04226c

rsc.li/nanoscale

Introduction

Superhydrophobic (SHB) surfaces constitute a type of material surface that demonstrates an exceptional ability to repel water. This distinctive property is most closely associated with the surface chemistry and morphological structure.[1] This remarkable characteristic has led to numerous applications within a broad range of industries. For instance, these applications entail the development of self-cleaning surfaces within the textile and automobile sectors,[2] the creation of anti-icing surfaces utilized by the aviation industry,[3] and corrosion-resistant surfaces for use in the marine industry.[4] Additional applications are found in the realm of electronic packaging for microelectronics[5,6] and solar-energy harvesters,[7] as well as the construction of anti-biofouling and other specialized surfaces for medical devices.[8] These diverse applications are anticipated to future technological innovations.

Black silicon (b-Si), a variant of silicon characterized by a distinctively textured surface and black color, has garnered considerable attention as a substrate for superhydrophobic surfaces.[9] Various fabrication techniques (*i.e.* reactive ion etching,[10] chemical etching,[11] laser[12]) have been utilized to generate the nanotexture of b-Si and their wetting properties have been thoroughly investigated.[13,14] Owing to its simple fabrication process, excellent superhydrophobic performance endowed by the air-filled structures, it has been utilized in numerous superhydrophobic applications. Moreover, thanks to compatibility with existing CMOS nanofabrication technologies, chemical inertness,[15] and low thermal conductivity,[16] b-Si has emerged as a prominent material in the realm of biomedical devices, particularly within microfluidic devices. It has been utilized to create anti-biofouling surfaces,[17] anti-bacterial surfaces,[18,19] and biofluid repellent surfaces.[20] Yet, akin to many superhydrophobic surfaces, b-Si surfaces are susceptible to issues with robustness due to their nanoscale-structured and rough texture. For instance, under conditions of high turbulence, strong fluid shear stresses can damage the nanostructures.[21] Efforts to enhance the robustness of superhydrophobic surfaces have been made;[22–24] however, there is sparse literature reporting on methods to increase the robustness of b-Si, indicating a compelling area for future research.

In this study, we report the development of a novel type of black silicon, nanojungle b-Si, which features extremely long and deep structures (over 10 μm). The nanojungle b-Si is fabricated using photoresist micromasks and Bosch etching techniques. Thanks to its deep nanostructures, the novel nanojungle b-Si surface, subsequent to surface modification, attained

[a]*Department of Applied Physics, Tietotie 3, Espoo, 02150, Finland.*
E-mail: lingju.meng@aalto.fi, sami.franssila@aalto.fi
[b]*Department of Chemistry and Materials Science, Tietotie 3, Espoo, 02150, Finland*
[c]*Micronova Nanofabrication Centre, Tietotie 3, Espoo, 02150, Finland*

† Electronic supplementary information (ESI) available. See DOI: https://doi.org/10.1039/d4nr04226c

superior superhydrophobic robustness compared to the traditional nanograss b-Si surface. This upgraded surface could withstand sand impact from a height of 40 cm. The factors contributing to this enhanced robustness were investigated *via* optical analysis, and key transition points of superhydrophobicity were identified and examined.

Nanojungle b-Si fabrication and characterization

To achieve the deep nanojungle structure, a novel nanofabrication route, utilizing Bosch etching assisted by micromasks was raised (Fig. 1a). This unique process began with a 100 mm prime Silicon (Si) wafer (p-type, ¡100¿, Siegert Wafer, Aachen, Germany). Initially, the Si wafer was coated with a layer of AZ 5214E photoresist (MicroChemicals GmbH, Ulm, Germany), acquired by spin-coating the wafer at a speed of 500 rpm (revolutions per minute) for the first 5 seconds and at 4000 rpm for the subsequent 40 seconds (Step b). Following spin-coating, the wafer was subjected to a hotplate soft baking step that lasted 2 minutes at a temperature of 90° to evaporate residual solvents from the photoresist film. The next step involves the use of Argon (Ar) milling *via* the reactive ion etching (RIE) technique (Oxford Plasmalab 80Plus), to make the photoresist surface rough (Step c). The process was performed with parameters of 30 mTorr pressure, 200 W power, 25 sccm CHF_3 flow and 25 sccm Ar flow. The duration of the etching can be adjusted as required to control the level of roughness on the photoresist surface, as shown in Fig. S1.† In this work, 30 min was chosen as the etching time.

Next, the sample with rough photoresist was introduced to an inductively coupled plasma etcher (ICP-RIE, Oxford Estrelas 100) for Bosch deep etching. This technique alternates among deposition (1.25s, ICP 1500 W, SF_6 10 sccm, C_4F_8 300 sccm, pressure 40 mTorr), breakdown (0.85s, ICP 1800 W, SF_6 200 sccm, C_4F_8 1 sccm, pressure 25 mTorr), and etching (0.85s, ICP 1800 W, SF_6 300 sccm, C_4F_8 10 sccm, pressure 50 mTorr) phases, producing high-aspect-ratio structures that resemble a 'nanojungle' on the Si wafer surface. During this etching process, the photoresist film underwent etching initially. After completing roughly 100 etching cycles, the photoresist film formed island-like configurations due to the surface's rough texture, serving as micro-masks for the subsequent Bosch deep etching process (Step d). It should be noted here that since the sample would be Bosch-etched all the way until the photoresist was completely stripped, there was no need to identify the exact time point when the micromasks were initially formed as shown in Step d. Owing to the high selectivity between AZ 5214E photoresist and Si,[25] the consecutive Bosch etching will result in an extremely deep, and high-aspect-ratio nanojungle b-Si structure. Hence, an additional 200 etching cycles were applied to achieve the desired nanojungle structure, as depicted in Step f. Because the micromasks were not flat structures (with bump-like structures), the resulting vertical structures would not be in perfect cylindrical structures (the area of

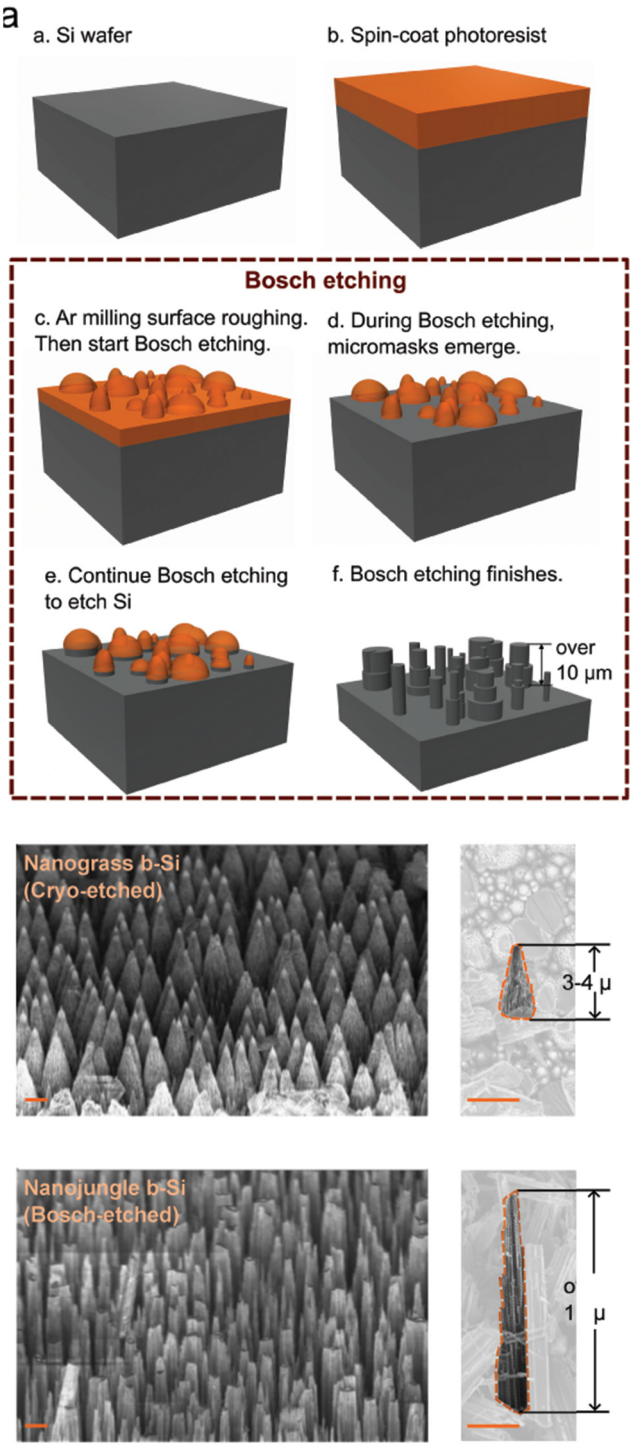

Fig. 1 (a) Nanofabrication process of the nanojungle b-Si. (b) SEM micrographs of vertically aligned nanograss and nanojungle b-Si structures (scale bar: 2 μm) and collapsed structure images of each kind (scale bar: 3 μm, top: nanograss b-Si, bottom: nanojungle b-Si).

the micromasks would gradually decrease during Bosch etching). Therefore, the strcutures would be needle-like random structures due to the bump-like micromasks. It is also noteworthy that Bosch etching might cause rough edges/surface on the micromasks. However, because the effect is sup-

posed to be negligible, the schematics in Fig. 1a does not reflect this change.

Finally, in order to achieve a superhydrophobic surface, a fluoropolymer layer was applied to the nanojungle structure using a plasma-enhanced chemical vapor deposition (PECVD) process carried out *via* the previously mentioned RIE system. The process was performed with parameters of 250 mTorr pressure, 50 W power, and 100 sccm CHF_3 flow for 5 min. It is worth noting that the fluoropolymer will create a proper surface chemistry towards superhydrophobicity. Bare b-Si surface will behave hydrophilic due to the existence of native oxide. Given the nano-textured rough surface, by different surface modification techniques (polymer deposition, self-assembled monolayer, *etc.*), the surface of b-Si can be tuned from superhydrophilic to superhydrophobic.[26]

Scanning electron microscopy (SEM) images of the resulting nanojungle b-Si and the reference nanograss b-Si were obtained using a Zeiss Supra 40 SEM system. These images, as depicted in Fig. 1b, demonstrate that both b-Si structures exhibit vertical configurations, albeit with distinct characteristics. A closer examination of the micrographs of the collapsed structures reveals that the lengths of the nanojungle structure, which extend over 10 μm, considerably surpass those of the nanograss structure, which reach 3–4 μm. It should be noted here that due to the limitation of the software, the random structures on the sidewalls of the nanojungles cannot be fully depicted in Step f of Fig. 1a. Please refer to Fig. 1b for details of the nanojungle structures. As what has been mentioned before, the nanojungle structure is needle-like random structures. The procedure for fabricating the nanograss b-Si, which has been adapted from previous literature,[20,27] is elaborated upon in the ESI.†

Experimental

The hydrophobicity of the samples was assessed using a contact angle meter (THETA, Biolin Scientifics, Espoo, Finland) with the needle in sessile droplet technique. Advancing contact angles were measured from 2 to 5 μL droplet size and receding angles from 5 to 0 μL with droplet pumping rate of 0.1 μL s^{-1}. The sand used in the impact test was from Biltema B.V., Sweden (size distribution: 200 μm–1 mm, product number: 175401). The optical images were obtained *via* an optical microscope (MX63L, Olympus, Tokyo, Japan). The reflectance spectra of the samples were measured using a Shimadzu UV-2600 UV-Vis spectrophotometer equipped with an ISR-2600Plus integrating sphere attachment (Shimadzu, Japan). Reflectance measurements were taken across wavelengths ranging from 300 nm to 900 nm.

Results and discussion

The contact angles of water on pristine nanograss b-Si and nanojungle b-Si were then acquired. The advancing and receding angles for the pristine nanograss b-Si surface were 173° and 170° respectively, compared to 166° and 159° for the pristine nanojungle b-Si surface. This data confirms the significant superhydrophobicity of both surfaces.

The robustness of samples was then evaluated by the sand impact test. As shown in Fig. 2a, the setup includes a funnel filled with a certain weight of sands positioned above the tested sample surface inclined at 45 degrees. Sand is allowed to fall from the funnel and impact the sample surface from varying heights.

Sand impact tests were carried out on both the nanograss and nanojungle b-Si superhydrophobic surfaces. The advancing and receding water contact angles were measured on both types of b-Si surfaces following exposure to sand impact from heights of 20 cm, 30 cm, and 40 cm, using a constant sand weight of 10 g. As shown in Fig. 2b and c, the novel nanojungle b-Si maintained high contact angles across all height conditions, indicating its superior robustness against sand impact. In contrast, the traditional nanograss b-Si exhibited a noticeable decrease in receding angles while the advancing

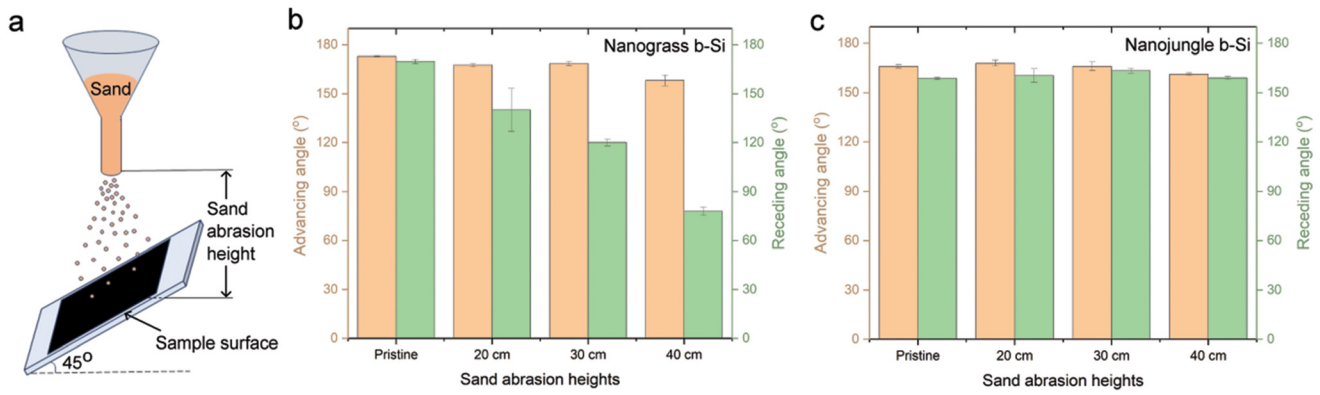

Fig. 2 Abrasion resistance of nanojungle b-Si (a) experimental setup of the sand impact test. (b) Contact angle measurement results of different nanograss b-Si surfaces after sand impact (10 g) from different heights. (c) Contact angle measurement results of different nanojungle b-Si surfaces after sand impact (10 g) from different heights. Bars represent standard deviation.

angles remained the same. This phenomenon means on the impacted nanograss b-Si surface, the contact angle hysteresis increased as sand abrasion height increased, suggesting a reduction in its superhydrophobic robustness.

To unveil the correlation between sand-impacted surface and superhydrophobicity, optical route was selected as the methodology. As shown in the left panel of Fig. 3a, incident light interacts with a vertical nanostructured surface – such as nanograss and nanojungle structures in a certain manner. The vertical structures trap and bounce photons between the nanostructures leading to an overall enhancement of light absorption, which appears as dark spots (low grayscale intensity) in optical images. Conversely, for collapsed structures (as shown in the right panel of Fig. 3a), the majority of incident light is reflected (both directly and diffusively) due to reduced internal reflections, leading to an overall increase in light reflectance and resultant bright spots in optical images (high grayscale intensity).

Consequently, optical micrographs of sand-impacted samples were captured. An example is shown in Fig. 3b, displaying evident bright (indicating reflection) and dark spots (indicating absorption). This contrast implies a heterogeneous surface where certain regions have preserved the nanostructural integrity (dark spots) while others have collapsed or been abraded (bright spots).

Histograms of pixel count *versus* grayscale intensity for sand-impacted nanograss and nanojungle b-Si superhydrophobic samples are presented in Fig. 3c and d respectively. For the nanograss sample (Fig. 3c), subjected to abrasive forces from three different sand drop heights (20 cm, 30 cm, and 40 cm), the number of pixels at the lower end of grayscale intensity – which represent vertical structures decreases as the height of sand abrasion increases. In contrast, the grayscale distribution of the pixel amounts for the nanojungle sample remains consistent across varying sand abrasion heights. Complete optical image set can be found as Fig. S2 in the ESI.†

Associating Fig. 3c and d with the contact angle measurements shown in Fig. 2b and c, it can be inferred that the collapse of nanograss structures indeed diminishes hydrophobicity. However, regarding the nanojungle b-Si surface, there is no observable change in either the pixel count distribution or the wetting property. This consistency reinforces the strong association that exists between surface morphology and wetting property.

With respect to the morphology, the prominent distinguishing feature between the nanojungle and nanograss structures lies in their depth. The nanograss structure is relatively shorter compared with the nanojungle structure. This shorter length results in higher stress concentration during the course of abrasion or impact. The localized stress at the fixed end due to the inability of the beam to flex will significantly increase the likelihood of the nanograss structure collapsing from the end. Once the nanograss structure is fully collapsed, it fails to generate sufficient roughness needed for the formation of the Cassie–Baxter state, in which the liquid does not penetrate into the hollows on the surface, creating an interface consisting of both solid and vapor.[28,29] Consequently, after enduring a certain degree of abrasion or impact, the superhydrophobicity of the nanograss b-Si structure diminishes, as depicted in the left panel of Fig. 4.

In contrast to shorter structures of nanograss b-Si, the deeper nanojungle structure demonstrates different behavior following abrasion or impact. The deep structure will be more flexible and will experience greater deflections under the same load compared to a short beam. The ability to flex and distribute stress reduces the chance of the nanojungle breaking at the end. While the long beam may still experience significant stress at the fixed end, the overall distribution of impact energy across the length of the structure lessens the peak stress at the end, increasing the likelihood of breaking in the middle. As demonstrated in the right panel of Fig. 4, the nano-

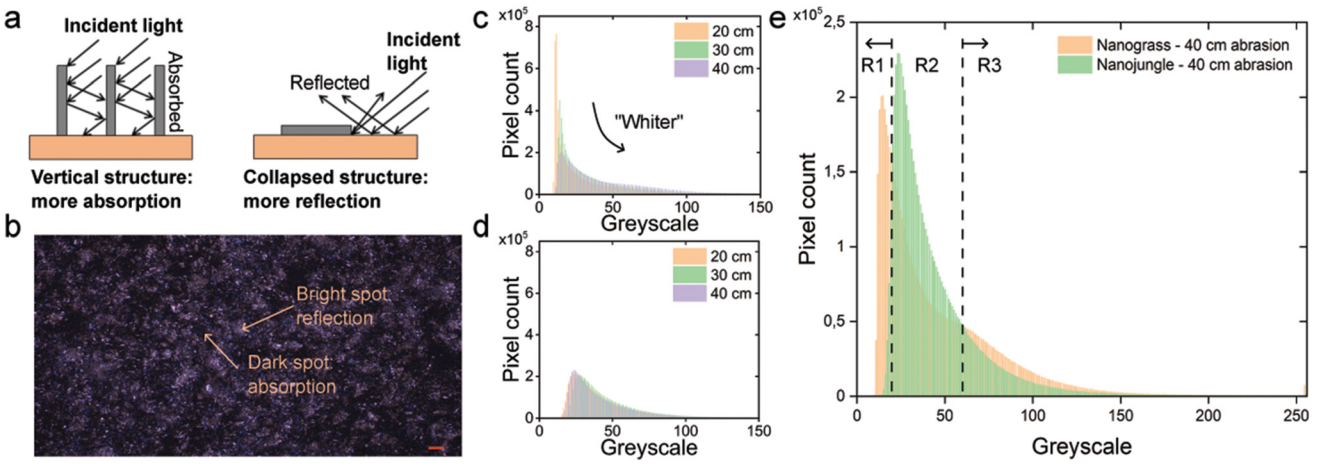

Fig. 3 Optical characterization of abrasion resistance (a) Schematics of interactions between incident light and vertical/collapsed structures. (b) Sample of optical micrograph of sand-impacted nanojungle b-Si surface. The scale bar in the graph is 100 μm. (c) Pixel count *vs.* grayscale histograms of nanograss b-Si samples impacted by sand from different heights. (d) Pixel count *vs.* grayscale histograms of nanojungle b-Si samples impacted by sand from different heights. (e) Pixel count *vs.* grayscale histograms of nanograss and nanojungle b-Si samples impacted by sand from 40 cm.

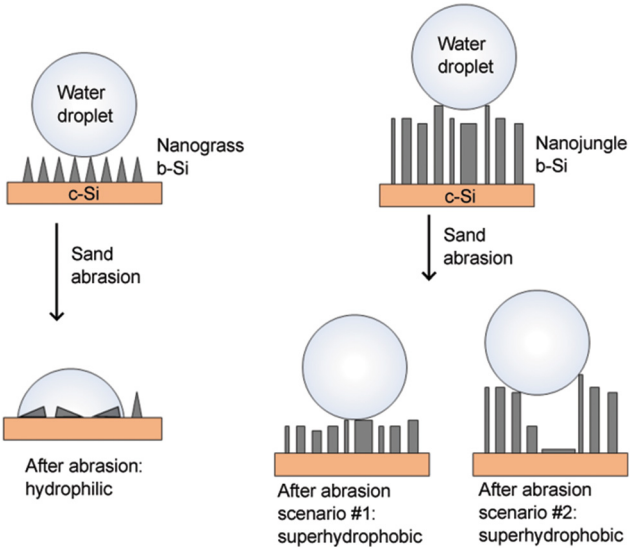

Fig. 4 Mechanisms for nanojungle b-Si superhydrophobic surface keeping its robustness towards superhydrophobicity.

jungle structure, given its tendency to break mid-way, ensures the remaining structures preserve sufficient roughness for superhydrophobicity following abrasion or impact. Even if micro-size areas (diameter smaller than the height of the nanojungle) of complete structural collapse occur on the surface, the deep nanojungle facilitates the effective air cushion necessary for the Cassie–Baxter state (Fig. 4). The evidence for these two scenarios was found on abrased/impacted nanojungle samples as shown in Fig. S4.†

To conclude, our novel nanojungle b-Si surface exhibits superior superhydrophobic robustness compared to the conventional nanograss b-Si surface owing to its deeply etched structures.

Notably, an observation can be made that the 'darker' pixels, representative of the vertical structures, are markedly greater on the nanograss surface compared to its nanojungle counterpart under the sand abrasion conditions, identified by weight and abrasion height, as shown in Fig. S3.† This phenomenon indicates that the long, jungle-like structures are easier to break under impact. We suspect that because long structures are more susceptible to buckling and may fail in modes other than brittle fracture. Despite this fact, the abrased nanojungle surface still maintain its superhydrophobic behavior. This observation thereby confirms the working mechanisms mentioned earlier.

To confirm this point, pixel histograms of both abraded surfaces resulting from the application of 10 g of sand from a height of 40 cm are presented in Fig. 3e for analysis. The histogram reveals three distinct regimes denoted as R1, R2, and R3. In R1 (approximately from grayscale 0 to 20) and R3 (approximately above grayscale 60), the nanograss pixels exhibit a higher frequency than those from the nanojungle sample, whereas in R2 (approximately from grayscale 20 to 60), nanojungle pixels outnumber those of the nanograss sample. This comparison can be interpreted as follows:

The R1 regime represents the fully intact vertical structures. As previously discussed, due to the buckling, the nanojungle is more easily broken, resulting in few nanojungle pixels in this regime.

The R3 regime comprises the 'brighter' pixels where the structures have been completely collapsed or removed. Due to the relatively shorter structures, the nanograss structure tends to be more fully removed or collapsed compared to the nanojungle structure, resulting in fewer nanojungle pixels in this regime.

Situated between R1 and R3 is R2, which can be characterized as the 'partially' collapsed conditions. These conditions can be understood as structures broken from the middle or micro-sized collapsed spots (smaller than the resolution of the microscope), resulting in grayscale levels between extreme brightness and darkness. The significantly larger population of nanojungle pixels in R2 serves as an indicator that the nanojungle structure has a tendency to maintain its superhydrophobicity, which suits the two 'after abrasion scenarios' as stated in the Working Mechanism Section and illustrated in Fig. 1c.

The reflectance spectra of the aforementioned samples were also obtained (Fig. S5†). By analyzing the spectra, it is evident that the reflectance of the traditional nanograss b-Si surface increased after abrasion, likely due to the collapse or complete removal of the nanograss structures. In contrast, the spectra of the nanojungle b-Si surface exhibited a decrease in post-abrasion reflectance, indicating enhanced absorption in the visible spectrum. This suggests that most nanojungle structures were only partially damaged, allowing them to retain their anti-reflective properties. The observed increase in absorption can be attributed to broken nanojungle debris, which may enhance photon scattering and bouncing between structures, thereby increasing absorption. The reflectance calculation method can be found in the ESI.†

In order to more comprehensively analyze the failure point of the nanojungle b-Si, sand impact tests using varying weights of sand from the same height, 40 cm, were put into effect. Fig. 5 illustrates the relationship between sand weight (g) and the advancing and receding contact angles on the nanojungle b-Si superhydrophobic surface.

The amber curve corresponds to the advancing contact angles, and the green curve corresponds to the receding contact angles. Both angles are initially high, indicating superhydrophobic behavior. As the sand weight increases, the advancing angle remains relatively stable, slightly decreasing but consistently above the superhydrophobic threshold. In contrast, the receding angle exhibits a significant decline after a sand weight of 30 g, transitioning from superhydrophobic (>150°) to hydrophobic and eventually becoming hydrophilic (<90°) at 60 g, indicating formation of Wenzel states, in which the water is in fully contact with the surface. The SEM micrographs (Fig. S6†) and pixel analysis (Fig. S7 and S8†) also elucidate the formation of Wenzel states due to large-area fully collapsed structures.

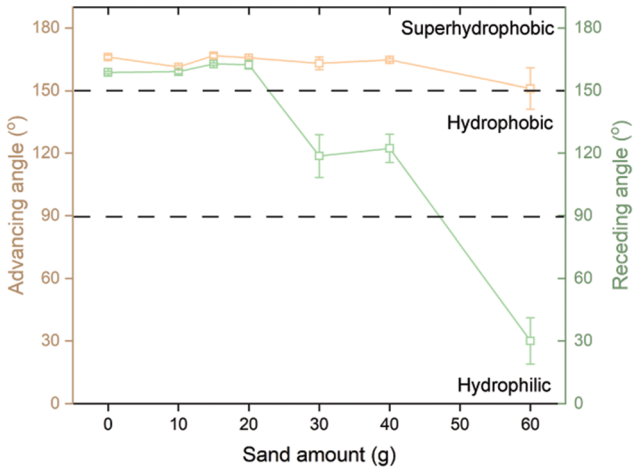

Fig. 5 Durability of superhydrophobicity of nanojungle b-Si as a function of sand weights.

Conclusions

In this study, we demonstrated the enhanced superhydrophobic robustness of the novel nanojungle b-Si surface compared to the traditional nanograss b-Si structure. The lengths of the nanojungle structures reach over 10 μm *via* a new fabrication route, Bosch etching assisted by micromasks. Through comprehensive sand impact testing and optical characterization, it was found that the nanojungle b-Si maintained high advancing and receding contact angles even after impact by sand from 40 cm, indicating superior robustness over nanograss b-Si. The enhanced robustness of the nanojungle b-Si can be attributed to its deeply etched structures, which are less prone to fully collapse and maintain their superhydrophobic properties even after impact. These findings suggest that nanojungle b-Si surfaces are more suitable for applications where long-term superhydrophobicity is critical, especially in environments subject to mechanical abrasion.

Data availability

Supplementary data are available in the ESI.† Other data that support the findings of this study are available from the corresponding author upon reasonable request.

Conflicts of interest

There are no conflicts to declare.

Acknowledgements

L. M. acknowledge funding from the European Union HE-MSCA-PF-2021 under grant agreement no. 101061892 (N2PCON). Funding from Research Council of Finland (#341459) is acknowledged. J. V. and M. Mousavi acknowledge the funding from project "PINT" from PREIN Flagship project (RCF decision number 346529). We also acknowledge the provision of facilities and technical support by Aalto University at Micronova Nanofabrication Centre and Nanomicroscopy Center.

References

1 X.-M. Li, D. Reinhoudt and M. Crego-Calama, *Chem. Soc. Rev.*, 2007, **36**, 1350–1368.
2 N. Tian, K. Chen, H. Yu, J. Wei and J. Zhang, *Iscience*, 2022, **25**, 104494.
3 D. Zeng, Y. Li, D. Huan, H. Liu, H. Luo, Y. Cui, C. Zhu and J. Wang, *Colloids Surf., A*, 2021, **628**, 127377.
4 R. Gupta, R. Verma, S. Kango, A. Constantin, P. Kharia, R. Saini, V. K. Kudapa, A. Mittal, J. Prakash and P. Chamoli, *Mater. Today Commun.*, 2023, **34**, 105201.
5 Y. Liu, Z. Lin, K. Moon and C. P. Wong, *IEEE Trans. Compon., Packag., Manuf. Technol.*, 2013, **3**, 1079–1083.
6 L. Li, Y. Bai, L. Li, S. Wang and T. Zhang, *Adv. Mater.*, 2017, **29**, 1702517.
7 H. Daghigh Shirazi, S. M. Mirmohammadi, S. M. Mousavi, M. Markkanen, J. Halme, V. Jokinen and J. Vapaavuori, *Commun. Mater.*, 2024, **5**, 88.
8 R. Kumar and A. K. Sahani, *Mater. Today: Proc.*, 2021, **45**, 5655–5659.
9 C. Dorrer and J. Rühe, *Adv. Mater.*, 2008, **20**, 159–163.
10 Z. Zhang, G. Liu and K. Wang, *Micromachines*, 2021, **12**, 1009.
11 R. C. Muduli, M. K. Sahoo and P. Kale, *Mater. Today: Proc.*, 2022, **62**, 5917–5922.
12 C. Yang, X. Jing, F. Wang, K. F. Ehmann, Y. Tian and Z. Pu, *Appl. Surf. Sci.*, 2019, **497**, 143805.
13 Y. A. Peschenyuk, A. A. Semenov, G. Y. Ayvazyan and E. Y. Gatapova, *Exp. Fluids*, 2023, **64**, 1.
14 G. Ayvazyan, L. Hakhoyan, A. Vardanyan, H. Savin and X. Liu, *Phys. Status Solidi RRL*, 2024, 2400072.
15 E. Mitsai, A. Kuchmizhak, E. Pustovalov, A. Sergeev, A. Mironenko, S. Bratskaya, D. Linklater, A. Balčytis, E. Ivanova and S. Juodkazis, *Nanoscale*, 2018, **10**, 9780–9787.
16 D. S. Smith, A. Alzina, J. Bourret, B. Nait-Ali, F. Pennec, N. Tessier-Doyen, K. Otsu, H. Matsubara, P. Elser and U. T. Gonzenbach, *J. Mater. Res.*, 2013, **28**, 2260–2272.
17 S. Turner, L. Kam, M. Isaacson, H. Craighead, W. Shain and J. Turner, *J. Vac. Sci. Technol., B:Microelectron. Nanometer Struct. – Process., Meas., Phenom.*, 1997, **15**, 2848–2854.
18 E. P. Ivanova, J. Hasan, H. K. Webb, G. Gervinskas, S. Juodkazis, V. K. Truong, A. H. Wu, R. N. Lamb, V. A. Baulin, G. S. Watson, *et al.*, *Nat. Commun.*, 2013, **4**, 2838.
19 D. P. Linklater, S. Juodkazis, S. Rubanov and E. P. Ivanova, *ACS Appl. Mater. Interfaces*, 2017, **9**, 29387–29393.

20 M. Awashra, P. Elomaa, T. Ojalehto, P. Saavalainen and V. Jokinen, *Adv. Mater. Interfaces*, 2024, **11**, 2300596.
21 J. Marlena, J. K. S. Tan, Z. Lin, D. X. Li, B. Zhao, H. L. Leo, S. Kim and C. H. Yap, *NPG Asia Mater.*, 2021, **13**, 58.
22 S. Liu, H. Zhou, H. Wang, Y. Zhao, H. Shao, Z. Xu, Z. Feng, D. Liu and T. Lin, *Adv. Mater. Interfaces*, 2017, **4**, 1700027.
23 D. Wang, Q. Sun, M. J. Hokkanen, C. Zhang, F.-Y. Lin, Q. Liu, S.-P. Zhu, T. Zhou, Q. Chang, B. He, *et al.*, *Nature*, 2020, **582**, 55–59.
24 W. Zhang, D. Wang, Z. Sun, J. Song and X. Deng, *Chem. Soc. Rev.*, 2021, **50**, 4031–4061.
25 M. Ashraf, S. V. Sundararajan and G. Grenci, *J. Micro/Nanolithogr., MEMS, MOEMS*, 2017, **16**, 034501–034501.
26 V. Liimatainen, A. Shah, L.-S. Johansson, N. Houbenov and Q. Zhou, *Small*, 2016, **12**, 1847–1853.
27 L. Sainiemi, V. Jokinen, A. Shah, M. Shpak, S. Aura, P. Suvanto and S. Franssila, *Adv. Mater.*, 2011, **23**, 122–126.
28 A. Cassie and S. Baxter, *Trans. Faraday Soc.*, 1944, **40**, 546–551.
29 A. Giacomello, S. Meloni, M. Chinappi and C. M. Casciola, *Langmuir*, 2012, **28**, 10764–10772.